Rigorous Three-Dimensional Photoresist Exposure and Development Simulation over Nonplanar Topography

Heinrich Kirchauer, *Student Member, IEEE*, and Siegfried Selberherr, *Fellow, IEEE*

***Abstract*— A rigorous three-dimensional (3-D) simulation method for photoresist exposure and development is presented in which light scattering due to a nonplanar topography is calculated using the Maxwell equations. The method relies on a Fourier expansion of the electromagnetic field and extends the two-dimensional (2-D) differential method [1], [2] to the third dimension. The model accounts for partial coherent illumination and considers the nonlinear bleaching reaction of the photoresist. For the development process, the cellular-based topography simulator of [3] has been extended. A detailed description of the theory behind the simulation method is presented, the computational efficiency is discussed, and simulation results are given.**

***Index Terms*—Nonplanar topography, photo lithography, resist development, resist exposure, rigorous electromagnetic scattering, three-dimensional simulation.**

I. Introduction

AMONG all technologies, photolithography holds the leading position in pattern transfer in today's semiconductor industry. The reduction of the lithographic feature sizes toward or even beyond the used wavelength and the increasing nonplanarity of the devices place considerable demands onto the lithography process. A better understanding of the fundamental physical effects governing submicrometer photolithography is necessary for further improvements.

One critical problem arises from the electromagnetic (EM) light scattering, caused by a nonplanar topography, which results in specular reflections into nominally unexposed regions of the photoresist. Rigorous solutions of this general scattering problem can be classified into time-domain and frequency-domain methods. In three dimensions representative examples are the time-domain finite-difference method that has been implemented on a massively parallel supercomputer [4]–[6], and the workstation-based waveguide model [7]–[9] that belongs to the frequency-domain methods.

Our approach corresponds to the three-dimensional (3-D) formulation of the differential method that was originally developed for the simulation of diffraction gratings [1] and adapted for two-dimensional (2-D) photolithography simulation in [2]. The differential method is based on a Fourier expansion of the EM field in the lateral coordinates and is therefore a frequency-domain method.

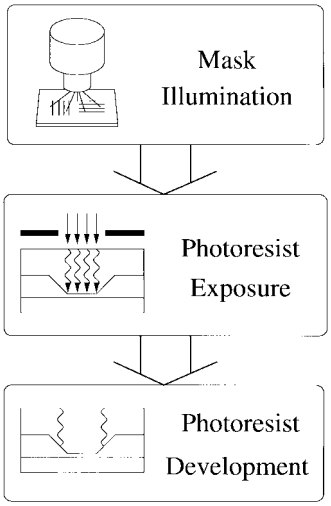

Fig. 1. Basic steps in photolithography simulation. Each module can be treated independently since well-defined interfaces exist.

This paper describes the 3-D extension of the differential method and its implementation on a common engineering workstation. In Section II, we give an overview of the overall simulation model including the vector-valued aerial image simulation and the exposure/bleaching model of the photoresist. In Section III, we present the 3-D formulation of the differential method focusing on our implementation and the numerical performance. Section IV describes the interface to the development/etching simulator of [3], and Section V contains some simulation results.

II. Simulation Model

The result of a photolithography simulator is the final developed resist profile. As shown in Fig. 1, the overall process can be divided into three major phases, namely imaging, exposure, and development [10]. Each of these steps requires its own specific simulation approach. Fortunately, well-defined interfaces exist between the three modules so that the involved physical phenomena can be treated independently. In this section, we describe the imaging part as it yields the input to the exposure simulation and give an overview of the exposure/bleaching model.

Manuscript received December 11, 1996. This work was supported by Austria Mikro Systeme International AG, Unterpremstätten, Austria and Christian Doppler Forschungsgesellschaft, Vienna, Austria. This paper was recommended by Associate Editor Z. Yu.

The authors are with the Institute for Microelectronics, Technical University Vienna, Gußhausstraße 27-29, A-1040 Vienna, Austria.

Publisher Item Identifier S 0278-0070(97)09360-3.

A. Imaging Simulation

Our aerial image simulator is based on a vector-valued extension [2], [11] of the scalar theory of Fourier optics [12]. The mask pattern is thereby assumed to be laterally periodic and the photo mask is infinitesimally thin with ideal transitions of the transmission characteristic. To account for partial coherent illumination or more general illumination forms like annular and quadrupole illumination, the distributed light source is discretized into mutually independent coherent point sources Q_{pq} [13]. The resulting image on top of the wafer, due to one coherent point source, can be expressed by a superposition of plane waves. For a numerically efficient exposure simulation, it is necessary that all the individual point source contributions are periodic as will be explained in Section III. Therefore, the spacing between the individual point sources Q_{pq} has to be chosen in a way that the lateral wavevector components $k_{x,p}$ and $k_{y,q}$ of the waves incident onto the mask equal an integer multiple of the sampling frequencies $2\pi/a$ and $2\pi/b$ in the Fourier domain, i.e.,

$$k_{x,p} = p\frac{2\pi}{a} \quad \text{and} \quad k_{y,q} = q\frac{2\pi}{b} \tag{1}$$

whereby a and b are the mask periods. This requirement is illustrated in the wavevector diagram of Fig. 2. Due to the periodicity of the EM field, the individual point source terms can be expressed by Fourier expansions

$$\begin{aligned} \boldsymbol{E}^{pq}(x,y,0) &= \sum_{n,m} \boldsymbol{E}^{pq}_{mn} e^{j2\pi(n/ax+m/by)} \\ \boldsymbol{H}^{pq}(x,y,0) &= \sum_{n,m} \boldsymbol{H}^{pq}_{nm} e^{j2\pi(n/ax+m/by)} \end{aligned} \tag{2}$$

which have the physical interpretation of a superposition of homogeneous plane waves with wavevectors $\boldsymbol{k}_{nm} = [k_{x,n}, k_{y,m}, \sqrt{k_0^2 - k_{x,n}^2 - k_{y,m}^2}]^{\mathrm{T}}$ and wavenumber $k_0 = 2\pi/\lambda_0$. The actinic wavelength is denoted by λ_0, and the time dependence of the EM field is a time-harmonic one, i.e., $\mathcal{E}(\boldsymbol{x};t) = \mathrm{Re}\{\boldsymbol{E}(\boldsymbol{x})e^{-j\omega_0 t}\}$ and $\mathcal{H}(\boldsymbol{x};t) = \mathrm{Re}\{\boldsymbol{H}(\boldsymbol{x})e^{-j\omega_0 t}\}$ with angular frequency $\omega_0 = 2\pi/(\sqrt{\varepsilon_0\mu_0}\lambda_0)$. The amplitudes of the electric and magnetic diffraction orders $\boldsymbol{E}^{pq}_{nm}$ and $\boldsymbol{H}^{pq}_{nm}$, respectively, follow from the vector-valued diffraction theory [2], [11]

$$\begin{aligned} \boldsymbol{E}^{pq}_{nm} &= T_{n-p,m-q}\boldsymbol{P}(n,m\colon p,q) \\ \boldsymbol{H}^{pq}_{nm} &= \frac{1}{k_0}\sqrt{\frac{\varepsilon_0}{\mu_0}}\boldsymbol{k}_{nm} \times \boldsymbol{E}^{pq}_{nm}. \end{aligned} \tag{3}$$

Here, T_{nm} stands for the Fourier coefficients of the mask transmission function. They are computed by first triangulating the piecewise constant transmission function and then superposing weighted analytical Fourier transforms of the triangular patterns. The second term $\boldsymbol{P}(n,m\colon p,q)$ in (3) is the vector-valued counterpart to the pupil function of the scalar diffraction theory [12] and follows from ray tracing through the optical system [2], [11]. $\boldsymbol{P}(n,m\colon p,q)$ is essentially a low-pass filter (no evanescent waves can travel toward the photoresist) and accounts for the polarization state, defocus, and higher order aberrations terms.

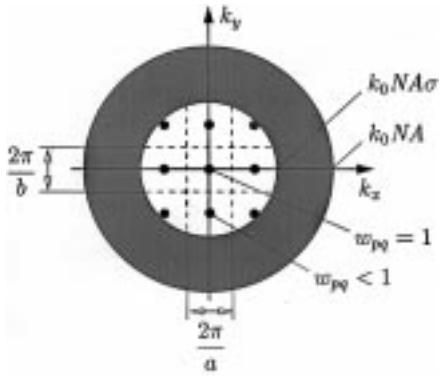

Fig. 2. To account for partial coherent illumination, the light source is discretized into mutually independent coherent point sources located inside the illumination cone. The radius $k_0 NA\sigma$ of the illumination cone is determined by the wavenumber $k_0 = 2\pi/\lambda_0$, the numerical aperture NA, and the partial coherence factor σ. The spacing between the individual point sources is chosen to yield a periodic incident EM field.

The aerial image itself is the light intensity $I(x,y)$ incident on top of the photoresist and, therefore, equals the real part of the vertical component of the Poynting vector of the EM field. It is calculated by a weighted incoherent superposition of the mutually independent terms and writes to

$$I(x,y) = \sum_{p,q} w_{pq}\,\mathrm{Re}[\boldsymbol{E}^{pq}(x,y,0) \times \boldsymbol{H}^{pq*}(x,y,0)]_z \tag{4}$$

whereby the asterisk denotes complex conjugation. For a uniform bright source, the weights w_{pq} are determined by the portion of the discretization area $2\pi/a \times 2\pi/b$ within the illumination cone (Fig. 2).

The Fourier coefficients of (3) are the input to the exposure/bleaching simulation, whereby it is important to point out, that the specific choice of the wavevector sampling in (1) results in a periodic incident field. This periodicity is essential for the efficient implementation of the differential method for multiple coherent point sources and will be further discussed in Section III.

B. Exposure/Bleaching Simulation

The exposure state of the photoresist is described by the photoactive compound (PAC) $M(\boldsymbol{x};t)$. Part of the incident photons of the exposing light are absorbed by the photoresist and destruct the PAC. Thereby, the resist's optical properties, e.g., the refractive index $n(\boldsymbol{x};t)$, are changed. We use Dill's "ABC" model[1] [14] to model the exposure/bleaching process

$$\begin{aligned} \frac{\partial M(\boldsymbol{x};t)}{\partial t} &= -CI(\boldsymbol{x};t)M(\boldsymbol{x};t) \\ n(\boldsymbol{x};t) &= n_0 + j\frac{\lambda}{4\pi}(AM(\boldsymbol{x};t) + B) \end{aligned}$$

where $I(\boldsymbol{x};t)$ is the exposing light intensity. The application of the Dill model in its original form is restricted to conventional positive photoresists. For chemically amplified resists, the photoactive compound generates a strong acid that has to be thermally activated after exposure. Such post-exposure bake steps are also applied in the case of conventional resists to smooth out variations in the bulk image of the PAC. In our

[1] Originally the Dill model was proposed for vertical field propagation only [14]. In [15] the model was extended to the general context of the macroscopic Maxwell equations.

application, we neglect this important processing step and use the relatively simple Dill model, as we are mainly interested in the impact of the EM field. However, the computation of the exposing EM field is relevant for any photoresist technique. Because the bleaching rate of all photoresists is small in comparison to the optical frequency, a quasi-static approximation can be applied, i.e.,

$$M(\boldsymbol{x};t_{k+1}) = M(\boldsymbol{x};t_k)e^{-CI(\boldsymbol{x};t_k),(t_{k+1}-t_k)} \tag{5}$$

whereby the initial PAC distribution is homogeneous $M(\boldsymbol{x};t_0) \equiv 1$. Furthermore, we assume a steady-state field distribution within a time step $t_k \leq t < t_{k+1}$. Therefore, the EM field is time-harmonic and obeys the Maxwell equations in the form of

$$\begin{aligned} \operatorname{curl} \boldsymbol{H}_k(\boldsymbol{x}) &= -j\omega_0\varepsilon_0\varepsilon_k(\boldsymbol{x})\boldsymbol{E}_k(\boldsymbol{x}) \\ \operatorname{curl} \boldsymbol{E}_k(\boldsymbol{x}) &= j\omega_0\mu_0\boldsymbol{H}_k(\boldsymbol{x}). \end{aligned} \tag{6}$$

The complex permittivity $\varepsilon_k(\boldsymbol{x})$ is related to the refractive index by Maxwell's law [16], $\varepsilon_k(\boldsymbol{x}) = n^2(\boldsymbol{x};t_k)$, and the exposing light intensity is given by [15]

$$I(\boldsymbol{x};t_k) = \frac{1}{2}\sqrt{\frac{\varepsilon_0}{\mu_0}}n_0\|\boldsymbol{E}_k(\boldsymbol{x})\|^2. \tag{7}$$

The equation set (5)–(7) represents the simulation model for the exposure/bleaching reaction, whereby an efficient solution of the Maxwell equations (6) is the crucial point for the applicability of the model. We propose the 3-D extension of the differential method [1], [2] as it can be implemented on a common engineering work station.

III. Three-Dimensional Differential Method

The simulation domain is one period $a \times b$ of a laterally periodic geometry. A typical formation is shown in Fig. 3. The vertical extension is chosen to comprise exactly the inhomogeneous photoresist and all nonplanar layer parts. The differential method itself can be divided into two stages. First, the dependence of the EM field on the lateral x- and y-coordinates is transformed into the frequency domain. Thereby, the partial differential equations are mapped onto a system of ordinary differential equations (ODE's). Once the boundary conditions (BC's) are determined and the ODE system is solved, the obtained field coefficients are transformed back to the spatial domain.

A. Lateral Discretization

Due to the periodic nature of the incident light (2) and the laterally periodic assumed simulation domain (Fig. 3), the EM field inside the simulation domain can be expressed by a Fourier expansion[2]

$$\begin{aligned} \boldsymbol{E}(x,y,z) &= \sum_{n,m}\boldsymbol{E}_{nm}(z)e^{j2\pi(nx/a+my/b)} \\ \boldsymbol{H}(x,y,z) &= \sum_{n,m}\boldsymbol{H}_{nm}(z)e^{j2\pi(nx/a+my/b)}. \end{aligned} \tag{8}$$

Here, it is most important to emphasize that the above expressions are valid independently of which point source Q_{pq} is chosen (Section II-A). That is why we can treat, for the moment, all incoherent contributions equivalently. The superscript pq is therefore omitted.

[2]For the sake of a compact notation we omit from now on the subscript k indicating the time step t_k.

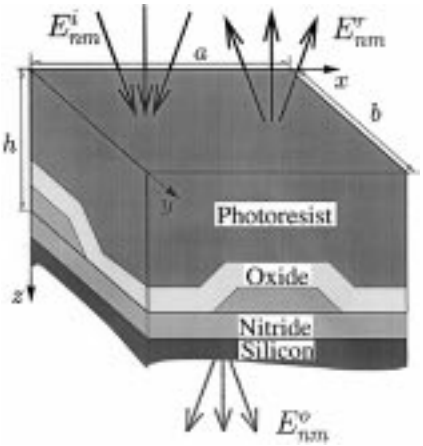

Fig. 3. The rectangular shaped simulation domain $(a \times b \times h)$ can contain arbitrary inhomogeneous and nonplanar regions. In the given example, the simulation domain consists of the inhomogeneous photoresist, the nonplanar oxide, and the nonplanar part of the nitride. Above $(z < 0)$ and below $(z > h)$ multiple planar homogeneous layers form a stratified medium that can be treated analytically.

Additionally, the inhomogeneous permittivity $\varepsilon(\boldsymbol{x})$ and its reciprocal $\chi(\boldsymbol{x}) = 1/\varepsilon(\boldsymbol{x})$ can be expanded in Fourier series[2]

$$\begin{aligned} \varepsilon(x,y,z) &= \sum_{n,m}\varepsilon_{nm}(z)e^{j2\pi(nx/a+my/b)} \\ \chi(x,y,z) &= \sum_{n,m}\chi_{nm}(z)e^{j2\pi(nx/a+my/b)}. \end{aligned} \tag{9}$$

Insertion of (8) and (9) into (6) transforms the partial differential equations into an infinite dimensional set of coupled ODE's for the Fourier coefficients of the lateral field components

$$\begin{aligned} \frac{dE_{x,nm}(z)}{dz} &= j\omega_0\mu_0 H_{y,mn}(z) + jn2\pi/aE_{z,nm}(z) \\ \frac{dE_{y,nm}(z)}{dz} &= -j\omega_0\mu_0 H_{x,nm}(z) + jm2\pi/bE_{z,nm}(z) \\ \frac{dH_{x,nm}(z)}{dz} &= -j\omega_0\varepsilon_0\sum_{r,s}\varepsilon_{n-r,m-s}E_{y,rs}(z) \\ &\quad + jn2\pi/aH_{z,nm}(z) \\ \frac{dH_{y,nm}(z)}{dz} &= j\omega_0\varepsilon_0\sum_{r,s}\varepsilon_{n-r,m-s}(z)E_{x,rs}(z) \\ &\quad + jm2\pi/bH_{z,nm}(z) \end{aligned} \tag{10}$$

with the vertical components given by

$$\begin{aligned} E_{z,nm}(z) &= -\frac{1}{\omega_0\varepsilon_0}\sum_{r,s}\chi_{n-r,m-s}(z) \\ &\quad \times [r2\pi/bH_{y,rs}(z) - s2\pi/bH_{x,rs}(z)] \\ H_{z,nm}(z) &= \frac{1}{\omega_0\mu_0}[n2\pi/aE_{y,nm}(z) - m2\pi/bE_{x,nm}(z)]. \end{aligned} \tag{11}$$

To solve this infinite dimensional ODE system numerically, the Fourier expansions are truncated, i.e., only coefficients

$\{E_{x,nm}, E_{y,nm}, H_{x,nm}, H_{y,nm}\}_{|n|\le N_x,|m|\le N_y}$ symmetrically centered around the principal incident ray $n = m = 0$ are considered. The introduced truncation error thus is not a simple low-pass filtering of the field due to the 2-D convolution-like relation of the Fourier coefficients (10) and (11). An analytical investigation of the truncation error is not straightforward, although qualitatively it is clear that the error increases with the inhomogeneity of the photoresist and the nonplanarity of the wafer topography. In the special case of a homogeneous photoresist and a planar substrate, no approximation error occurs at all. Numerical investigations have shown that above a certain truncation level the solution converges and additional Fourier coefficients do not alter the result significantly. For an isolated feature over a nonplanar geometry a typical value for the cutoff frequency is $N_x = N_y = 15$. However, our approach is practicable for smooth geometries only, because otherwise the number of relevant Fourier coefficients becomes too large.

Next, we rewrite (10) using a matrix-vector notation

$$\frac{d}{dz}\boldsymbol{u}(z) = \underline{\boldsymbol{H}}(z)\cdot\boldsymbol{u}(z) \quad \text{with} \quad \underline{\boldsymbol{H}}(z) = \begin{bmatrix} \underline{\mathbf{0}} & \underline{\boldsymbol{R}}(z) \\ \underline{\boldsymbol{G}}(z) & \underline{\mathbf{0}} \end{bmatrix}. \tag{12}$$

The complex-valued vector $\boldsymbol{u}(z) = [\boldsymbol{e}_x(z), \boldsymbol{e}_y(z), \boldsymbol{h}_x(z), \boldsymbol{h}_y(z)]^{\mathrm{T}}$ comprises the Fourier coefficients of the lateral field components, e.g., $(\boldsymbol{e}_x(z))_k = E_{x,n(k)m(k)}(z)$, and the elements $\underline{\boldsymbol{R}}(z)$ and $\underline{\boldsymbol{G}}(z)$ of the system matrix $\underline{\boldsymbol{H}}(z)$ contain the Fourier coefficients of the permittivity $\varepsilon(\boldsymbol{x})$ and its reciprocal $\chi(\boldsymbol{x})$. Each of the $\boldsymbol{e}$ and $\boldsymbol{h}$ vectors has dimension $(2N_x+1)\times(2N_y+1)$ due to the symmetric truncation of the Fourier sums. Therefore the entire ODE system is of dimension

$$\begin{aligned} N_{\mathrm{ODE}} &= 4\times(2N_x+1)\times(2N_y+1) \\ &\approx 16\times N_x\times N_y. \end{aligned} \tag{13}$$

Furthermore, the special structure of the system matrix in (12) is worth mentioning. The derivative of the $\boldsymbol{e}$ vectors is only related to the $\boldsymbol{h}$ vectors, and vice versa, which directly follow from the Maxwell equations (6). Consideration of this property relaxes the memory requirements and computational demands for the numerical solution of the ODE system. As the BC's of the ODE system are decisive for the choice of the numerical solution algorithm, we will discuss them next.

B. Boundary Conditions

Above and below the simulation domain we have homogeneous planar layers (Fig. 3). Inside one layer the EM field can be expressed by a plane wave or Rayleigh expansion [16]. The mathematical formulation is that of a Fourier expansion with vertically known dependence of the coefficients (Section II-A). Above the simulation domain $(z<0)$ we have to consider incident and reflected waves

$$\begin{aligned} \boldsymbol{U}(x,y,z) = \sum_{\substack{|n|\le N_x \\ |m|\le N_y}} &\left[\boldsymbol{U}^i_{nm} e^{jk^0_{z,nm}z} + \boldsymbol{U}^r_{nm} e^{-jk^-)z,nmz}\right] \\ &\times e^{j2\pi(nx/a+my/b)} \end{aligned} \tag{14}$$

below $(z>h)$ only outgoing waves occur disregarding multiple planar layers

$$\boldsymbol{U}(x,y,z) = \sum_{\substack{|n|\le N_x \\ |m|\le N_y}} \boldsymbol{U}^0_{nm} e^{jk^s_{z,nm}z} e^{j2\pi(nx/a+my/b)} \tag{15}$$

whereby $\boldsymbol{U}$ stands vicariously for both EM field vectors $\boldsymbol{E}$ and $\boldsymbol{H}$. The extension to the general situation of a vertically stratified medium is straightforward [16] and therefore skipped in this article. Matching the two Rayleigh expansions (14) and (15) with the field representation (8) valid inside the simulation domain, and eliminating the unknown reflected and outgoing wave amplitudes $\boldsymbol{U}^r_{nm}$ and $\boldsymbol{U}^o_{nm}$, respectively, yield exactly half of the BC's at the top $(z=0)$ and at the bottom $(z=h)$ of the simulation domain. The incident amplitudes $\boldsymbol{U}^i_{nm}$ are of course involved in the BC's as they excite the EM field inside the simulation domain. They are the output of the illumination simulation, and given by (3). This means that we have different BC's for each coherent point source. Using the above introduced vector notation we find

$$\underline{\boldsymbol{B}}_0\cdot\boldsymbol{u}(0) = \boldsymbol{a}^{pq} \quad \text{and} \quad \underline{\boldsymbol{B}}_h\cdot\boldsymbol{u}(h) = \mathbf{0}. \tag{16}$$

The two rectangular matrices $\underline{\boldsymbol{B}}_0$ and $\underline{\boldsymbol{B}}_h$ are independent of the chosen point source, whereas the vector $\boldsymbol{a}^{pq}$ comprises the incoming wave amplitudes $\boldsymbol{E}^{pq}_{nm}$ and $\boldsymbol{H}^{pq}_{nm}$ of one coherent point source contribution (3). This means that we have transformed the Maxwell equations (6) into a linear complex-valued two-point boundary value problem (12), (16) with multiple BC's.

C. Vertical Discretization

We adapted the memory saving "shooting method" [17] as it allows a very efficient treatment of the multiple right-hand sides of the first BC in (16). The algorithm is based on the observation that the system matrix $\underline{\boldsymbol{H}}(z)$ in (12) as well as the two boundary matrices $\underline{\boldsymbol{B}}_0$ and $\underline{\boldsymbol{B}}_h$ of (16) are independent of the chosen point source Q_{pq}. Exploiting this situation, we first establish a relation between the two boundary points $z=0$ and $z=h$. This is accomplished by applying an explicit discretization scheme to (12). The obtained recursion formula $\boldsymbol{u}(z_{j+1}) = \underline{\boldsymbol{S}}_j\cdot\boldsymbol{u}(z_j)$ between two adjacent mesh points z_j and $z_{j+1} = z_j + h_j$ is then successively evaluated

$$\boldsymbol{u}(h) = \left[\prod_{j=0}^{N_z-1}\underline{\boldsymbol{S}}_j\right]\cdot\boldsymbol{u}(0) = \underline{\boldsymbol{S}}\cdot\boldsymbol{u}(0) \tag{17}$$

whereby N_z is the number of vertical discretization points. Combining this equation with the second BC of (16) yields $\underline{\boldsymbol{B}}_h\cdot\boldsymbol{u}(h) = \underline{\boldsymbol{B}}_h\cdot\underline{\boldsymbol{S}}\cdot\boldsymbol{u}(0) = \mathbf{0}$, which forms together with the first BC of (16) a linear algebraic system for the initial values $\boldsymbol{u}^{pq}(0)$ due to one excitation vector $\boldsymbol{a}^{pq}$

$$\begin{bmatrix} \underline{\boldsymbol{B}}_0 \\ \underline{\boldsymbol{B}}_h\cdot\underline{\boldsymbol{S}} \end{bmatrix}\cdot\boldsymbol{u}^{pq}(0) = \begin{bmatrix} \boldsymbol{a}^{pq} \\ \mathbf{0} \end{bmatrix}. \tag{18}$$

This linear system is solved by performing an LU decomposition, which is an extremely efficient solution method for linear systems with multiple right-hand sides [18]. Once the

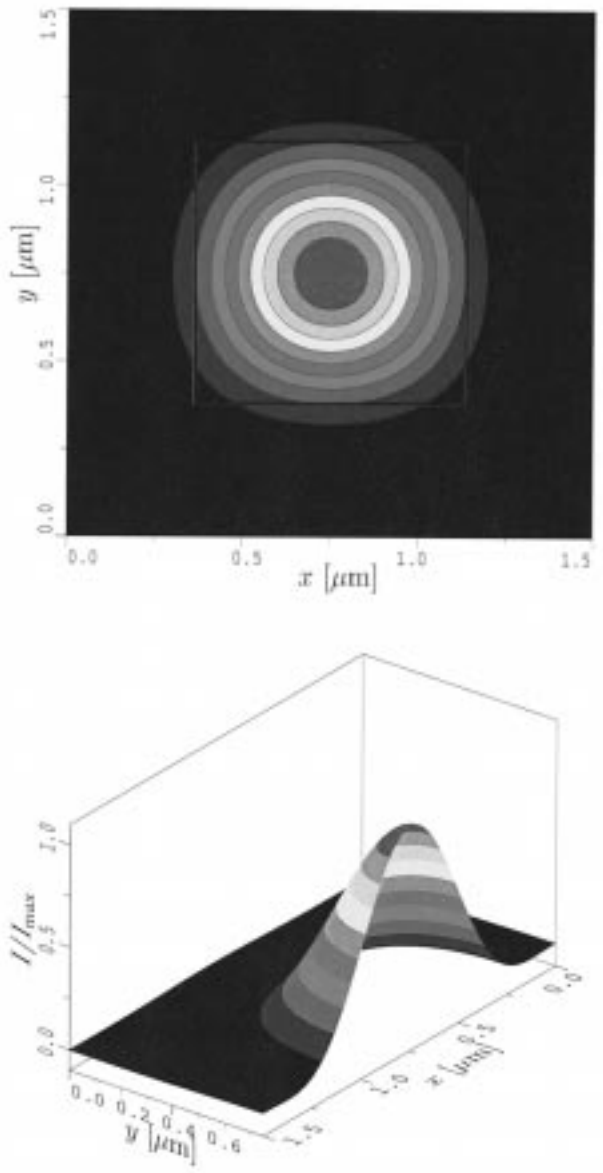

Fig. 4. Aerial image of a 0.75 μm $\times$ 0.5 μm wide contact hole centered in the middle of the 1.5 μm $\times$ 1.5 μm large simulation domain.

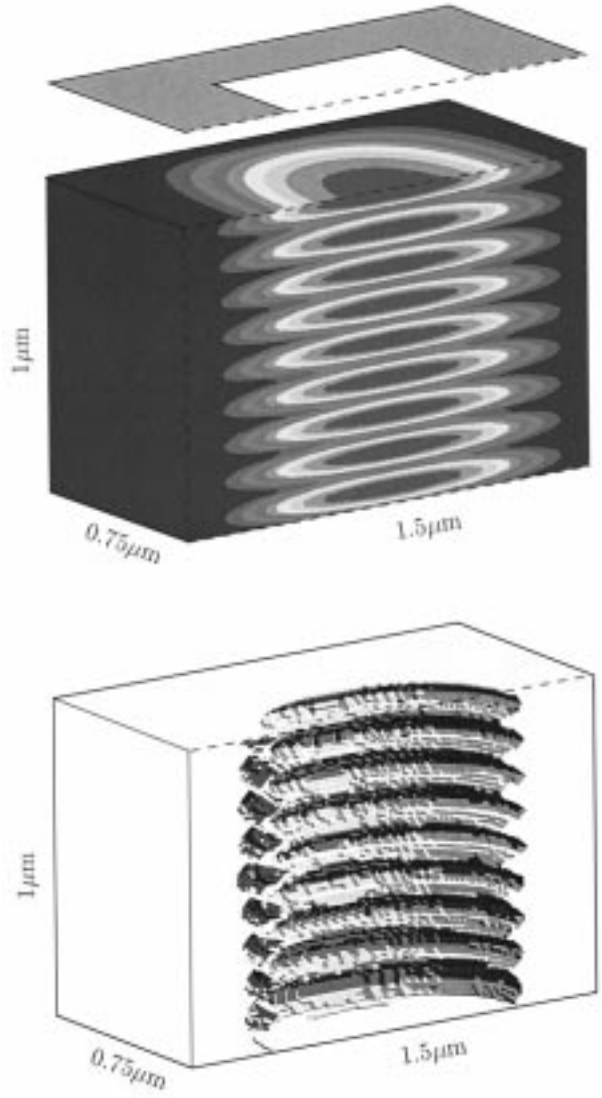

Fig. 5. Contour plot of the PAC and developed photoresist profile over a planar substrate. The oval contours are caused by standing waves within the photoresist which result from substrate reflections.

initial values $\boldsymbol{u}^{pq}(0)$ are found, the solution vector $\boldsymbol{u}^{pq}(z_j)$ inside the simulation domain is calculated by integrating the ODE system (12). As the elements of $\boldsymbol{u}^{pq}(z_j)$ correspond to the Fourier coefficients of the EM field, they have to be transformed back to the spatial domain. Finally, the point source contributions are incoherently superposed to build up the absorbed light intensity within the photoresist needed in (7) for the exposure/bleaching model.

D. Computational Efficiency

The proposed algorithm has the big advantage that the vertical mesh size N_z does not influence the storage consumption as the recursion matrices $\underline{\boldsymbol{S}}_j$ in (17) do not have to be stored individually. The memory usage is therefore only determined by the rank N_{ODE} of the ODE system (13) and is of order $\mathcal{O}(N_{\mathrm{ODE}}^2) \approx 256 \times \mathcal{O}(N_x^2 \times N_y^2)$. Typically 30 Fourier coefficients are needed for each lateral direction. In this case, $N_x = N_y = 15$, the ODE system is of rank $N_{\mathrm{ODE}} = 3844$. Assuming 16 bytes for a double precision complex number, approximately 250 MB of memory are required to store the system matrix. For a 3-D rigorous photolithography simulation, this storage consumption is in accordance with other frequency-domain methods, e.g., [9], and lies dramatically below time-domain methods, e.g., [6].

For the investigation of the numerical costs, we have to bear in mind that the Maxwell equations (6) have to be solved for multiple time steps (Section II-B). The numerical costs for one time step are mainly determined by the evaluation of the recursion (17) and by the solution of (18). Both operations are of order $\mathcal{O}(N_{\mathrm{ODE}}^3)$. Hence, the total run time grows for N_t time steps and N_z vertical discretization points with $\mathrm{O}(N_t \times N_z \times N_{\mathrm{ODE}}^3)$, and is typically under a few hours on a DEC-600 workstation.

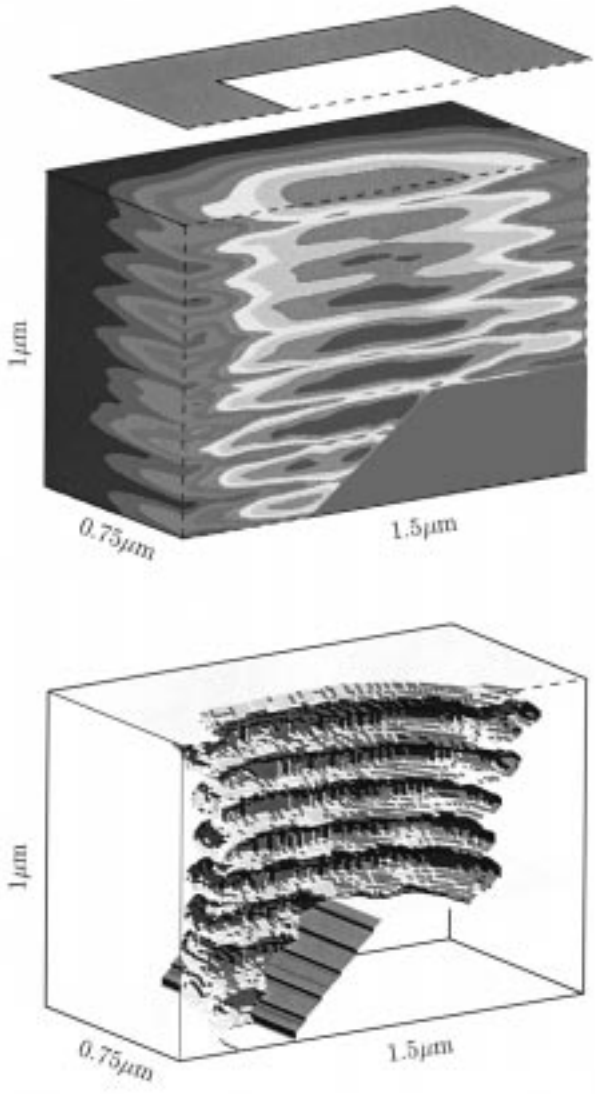

Fig. 6. Contour plot of the PAC and developed photoresist profile over a dielectric oxide step and silicon bulk. Due to the variation in optical thickness, the oval contours are distorted as compared to Fig. 5. Certain regions within the photoresist are overexposed.

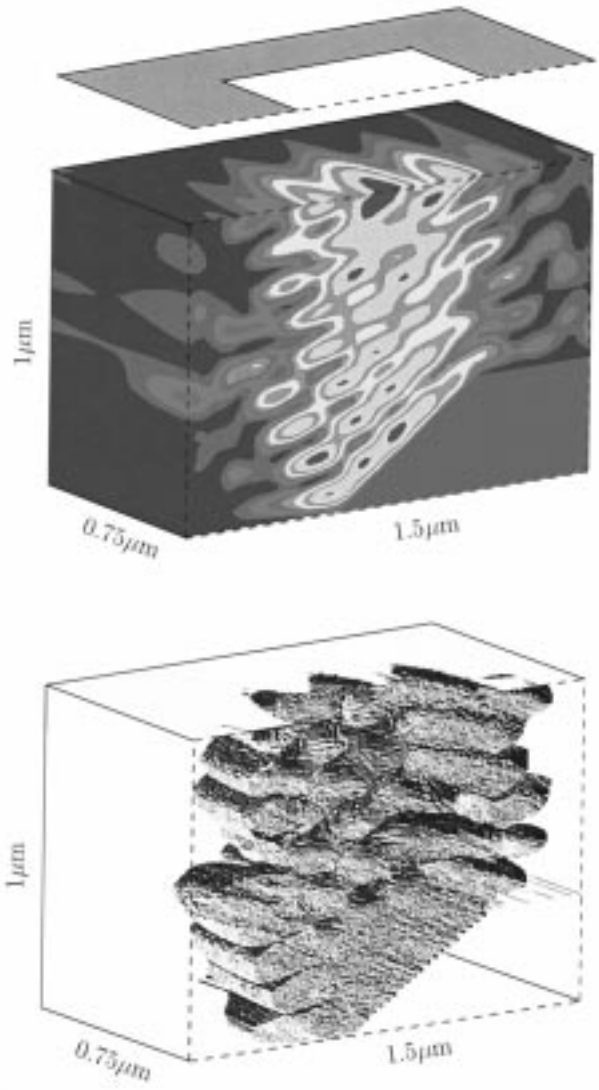

Fig. 7. Contour plot of the PAC and developed photoresist profile over a silicon step. The reflective silicon forces a node in the intensity distribution along the surface of the step. Thus, the impact of the nonplanarity is more severe than in Fig. 6.

IV. Development Simulation

The development of the photoresist is modeled as a surface-controlled etching reaction [14]. We use Kim's "R" model to relate the final PAC distribution of the exposure/bleaching simulation to a spatially inhomogeneous etch or development rate [19]. This development rate is stored on a tensor product grid because the above discussed differential method requires a laterally uniformly spaced grid to apply the numerically highly efficient 2-D fast fourier transform (FFT) algorithm. For the simulation of the time evolution of the development front, we have adapted the recently proposed cellular-based topography simulator of [3] and [20] to read the development rate from the tensor product grid. The basic idea behind this surface advancement algorithm is to apply a structuring element along the exposed surface which removes successively photoresist cells of the underlying cellular geometry representation. Within the scope of lithography simulation, the shape of the structuring element depends on the precalculated development rate multiplied by the chosen time step. As the development rate exhibits a strong dependence on the spatial coordinates, e.g., due to standing waves or notching effects during photoresist exposure, a sufficiently high number of cells has to be chosen to resolve these variations.

For example, in case of standing waves, we know that the distance between the maxima and minima of the absorbed light intensity, and therefore, also of the development rate, is $\lambda/4$ yielding approximately 50 nm for I-line illumination ($\lambda = 365$ nm) and a refractive index of 1.8 for the photoresist. For an accurate movement of the development front, this significant distance should be resolved by 15 cells [3]. Hence a cell density of 300 cells/μm is needed. The applicability of the advancement algorithm for this cellular geometry resolution has been demonstrated in [3].

V. Simulation Results

To demonstrate the capability of our approach, we simulated contact hole printing over a planar and a stepped topography

(Figs. 4–7). In all cases, the simulation domain was 1.5 μm $\times$ 1.5 μm $\times$ 1.0 μm large, and the bulk material underneath was silicon with a refractive index of $n_{\mathrm{Si}} = 6.522 + j2.705$. In the nonplanar cases, the step was centered in the middle of the simulation domain, the height was 0.33 μm and the slope was 45°. In Fig. 6, the step material was oxide with a refractive index of $n_{\mathrm{SiO_2}} = 1.475$, and in Fig. 7 silicon was used throughout.

For the imaging and exposure/bleaching simulation, 31 Fourier modes or $N_x = N_y = 15$ were used to represent the EM field consuming 250 MB memory. The number N_z of vertical discretization points was 100 and five time steps were used for the bleaching reaction. The run time was about six hours on DEC-600 workstation.

The development simulation was performed with a cell density of 300 cells/μm. The memory usage was 60 MB assuming 1 byte per cell and the run time was 30 minutes on a DEC-600 workstation.

In Fig. 4, we show the aerial image obtained by the vector-valued approach discussed in Section II-A. Conventional I-line illumination with a numerical aperture of $NA = 0.5$ and a partial coherence factor of $\sigma = 0.7$ was used. Nine mutually incoherent point sources were needed to account for the partial coherence. The point source location is shown in the wavevector diagram of Fig. 2.

In Figs. 5–7, a contour plot of the PAC is shown in the upper picture and the developed photoresist profile in the lower picture. The simulation of the post-exposure bake step was omitted because the original shape of the EM field and its plain influence on the resist profile should be demonstrated. The post-exposure bake can easily be accounted for by a diffusion simulation with constant diffusion coefficient [21]. The contours are given for PAC $= 0.2, 0.3, \cdots, 1.0$. The exposure dose was 120 mJ/cm^2 and the development time was 50 s. The simulation parameters were for the Dill-model $n_0 = 1.65, A = 0.55$ μm$^{-1}, B = 0.045$ μm$^{-1}, C = 0.013$ cm^2/mJ, and for the Kim model $R_1 = 0.25$ μm/s, $R_2 = 0.0005$ μm/s, $R_3 = 7.4$ [19, Table IV].

A comparison of the simulations exhibits a wider opening in the developed photoresist for the stepped topographies in Figs. 6 and 7 than for the planar substrate in Fig. 5. Hence, the effective diameter of the contact hole depends on the nonplanarity of the wafer topography. This dependence is stronger for the reflective silicon than for the dielectric oxide. The standing waves, and thus the resist profiles, are also more conformal along the step in Fig. 7 than in Fig. 6.

Further comparisons with experiments are not presented, as the main scope of this article is to formulate the 3-D differential method and to demonstrate its applicability for rigorous 3-D work station based photolithography simulation. The intrinsic physical correctness of the differential method for photolithographic applications has already been demonstrated in two dimensions [2] and can therefore be taken for granted.

The fundamental tradeoff between computational demands and accuracy can best be seen by considering the proposed wave-vector sampling in (1). Too small periods a and b in proportion to the wavelength λ yield a coarse grid not suited to describe the physical phenomena adequately. On the other hand, as the number N_x and N_y of required Fourier coefficients increases proportionally to a/λ and b/λ, respectively, the method is limited by its computational requirements in case of too large periods a and b. The given simulations of this crucial ratio was four, which seems to be a reasonable compromise.

VI. Conclusion

The 2-D differential method was extended to the third dimension. The 3-D formulation was presented, and it was shown that the approach is extremely efficient to account for partial coherent illumination. The method was implemented on a common engineering workstation and embedded in the exposure/bleaching part of an overall photolithography simulation program. The interface to the two other parts, namely the vector-valued aerial image calculation and the development/etching simulator, was described. The capability of the approach was demonstrated by showing simulation results of contact hole printing over a planar and nonplanar topography.

References

[1] R. Petit, *Electromagnetic Theory of Gratings*. Berlin, Germany: Springer-Verlag, 1980.

[2] M. S. Yeung, "Modeling high numerical aperture optical lithography," in *Proc. SPIE Optical/Laser Microlithography*, vol. 922, 1988, pp. 149–167.

[3] E. Strasser and S. Selberherr, "Algorithms and models for cellular based topography simulation," *IEEE Trans. Computer-Aided Design*, vol. 14, pp. 1104–1114, Sept. 1995.

[4] R. Guerrieri, K. H. Tadros, J. Gamelin, and A. R. Neureuther, "Massively parallel algorithms for scattering in optical lithography," *IEEE Trans. Computer-Aided Design*, vol. 10, pp. 1091–1100, Sept. 1991.

[5] A. K. Wong, R. Guerrieri, and A. R. Neureuther, "Massively parallel electromagnetic simulation for photolithographic applications," *IEEE Trans. Computer-Aided Design*, vol. 14, pp. 1231–1240, Oct. 1995.

[6] A. K. Wong and A. R. Neureuther, "Rigorous 3-D time-domain finite-difference electromagnetic simulation for photolithographic applications," *IEEE Trans. Semiconduct. Manufact.*, vol. 8, pp. 419–431, Nov. 1995.

[7] C. M. Yuan, "Efficient light scattering modeling for alignment, metrology, and resist exposure in photolithography," *IEEE Trans. Electron Devices*, vol. 39, pp. 1588–1598, July 1992.

[8] H. Tanabe, "Modeling of optical images in resists by vector potentials," in *Proc. SPIE Optical/Laser Microlithography V*, vol. 1674, 1992, pp. 637–649.

[9] K. D. Lucas, H. Tanabe, C. M. Yuan, and A. J. Strojwas, "Efficient and rigorous 3-D model for optical lithography simulation," in *Proc. SISDEP-95*, vol. 6, pp. 14–17, 1995.

[10] K. K. H. Toh and A. R. Neureuther, "3-D simulation of optical lithography," in *Proc. SPIE Optical/Laser Microlithography IV*, vol. 1463, 1991, pp. 356–367.

[11] E. Wolf, "Electromagnetic diffraction in optical systems I. An integral representation of the image field," *Proc. Royal Soc. London*, vol. A-253, pp. 349–357, 1959.

[12] J. W. Goodman, *Introduction to Fourier Optics*. New York: McGraw-Hill, 1968.

[13] H. P. Urbach and D. A. Bernard, "Modeling latent-image formation in photolithography, using the Helmholtz equation," *J. Opt. Soc. Amer. A, Opt. Image Sci.*, vol. 6, no. 9, pp. 1343–1356, Sept. 1989.

[14] F. H. Dill, "Optical lithography," *IEEE Trans. Electron Devices*, vol. ED-22, no. 7, pp. 440–444, July 1975.

[15] D. A. Bernard, "Simulation of focus effects in photolithography," *IEEE Trans. Semiconduct. Manufact.*, vol. 1, no. 3, pp. 85–97, Aug. 1988.

[16] M. Born and E. Wolf, *Principles of Optics*, 6th ed. Oxford: Pergamon, 1993.

[17] U. M. Ascher, R. M. M. Mattheij, and R. D. Russell, "Numerical solution of boundary value problems for ordinary differential equations," in *Classics in Applied Mathematics*. Philadelphia: SIAM, vol. 13, 1995.

[18] G. H. Golub and C. F. Van Loan, *Matrix Computations*, 2nd ed. Baltimore: Johns Hopkins, 1989.
[19] D. J. Kim, W. G. Oldham, and A. R. Neureuther, "Development of positive photoresist," *IEEE Trans. Electron Devices*, vol. ED-31, no. 12, pp. 1730–1736, Dec. 1984.
[20] E. Strasser, G. Schrom, K. Wimmer, and S. Selberherr, "Accurate simulation of pattern transfer processes using Minkowski operations," *IEICE Trans. Electron*, vol. E77-C, pp. 92–97, 1994.
[21] E. J. Walker, "Reduction of photoresists standing-wave effects by post-exposure bake," *IEEE Trans. Electron Devices*, vol. ED-22, no. 7, pp. 464–466, July 1975.

Heinrich Kirchauer (SM'94) was born in Vienna, Austria, in 1969. He studied communications engineering at the Technical University Vienna, Austria, where he received the degree of Diplomingenieur in March 1994. In December 1994, he joined the Institut für Mikroelektronik, Technical University Vienna, where he is currently working toward the Ph.D. degree.

After his Master's studies he spent the next six months at the Technical University Vienna, involved in a research project on statistical signal processing. In the summer of 1997, he held a visiting research position at LSI Logic, Milpitas, CA, USA. His scientific interests include three-dimensional process simulation with special emphasis on lithography simulation.

Siegfried Selberherr (M'79–SM'84–F'93) was born in Klosterneuburg, Austria, in 1955. He received the degree of Diplomingenieur in electrical engineering and the Ph.D. degree in technical sciences from the Technical University Vienna, Austria, in 1978 and 1981, respectively.

Since that time, he has been a Professor with the Technical University Vienna. He has been holding the "venia docendi" on computer-aided design since 1984, and has been Head of the Institut für Mikroelektronik since 1988. His current interests include modeling and simulation of problems for microelectronics engineering.